Petroleum Science 21 (2024) 1524–1538

Contents lists available at ScienceDirect

Petroleum Science

journal homepage: www.keaipublishing.com/en/journals/petroleum-science

Original Paper

Microfacies and diagenetic alteration in a semi-deep to deep lacustrine shale: The Yanchang Formation in the Ordos Basin, China

Bin Bai [a, *], Jing-Yue Hao [b], Ling Fu [a], Yu-Xi Liu [a], Jian-Peng Wang [b, c, **], Lan Wang [a], Kevin G. Taylor [b], Lin Ma [d]

[a] PetroChina Research Institute of Petroleum Exploration and Development, Beijing, 100083, China
[b] Department of Earth and Environmental Sciences, University of Manchester, Manchester, M13 9PL, UK
[c] College of Earth Sciences, Jilin University, Changchun, 130061, Jilin, China
[d] Department of Chemical Engineering, University of Manchester, Manchester, M13 9PL, UK

ARTICLE INFO

Article history:
Received 5 April 2023
Received in revised form
16 October 2023
Accepted 27 December 2023
Available online 8 January 2024

Edited by Jie Hao and Meng-Jiao Zhou

Keywords:
Ordos Basin
Yanchang Formation
Chang 7 Member
Diagenesis
Microfacies

ABSTRACT

The mineralogical development and diagenetic sequence of lacustrine shales in the Chang 7 Member of the Yanchang Formation in the Ordos Basin are detailed studied. A model of their depositional system and a diagenetic diagram are proposed in this study. Through detailed petrographic, mineralogical, and elemental analyses, four distinct shale types are identified: argillaceous shale, siliceous shale, calcareous shale, and carbonate, clay, and silt-bearing shale. The main diagenetic process in argillaceous shale is the transformation of illite to smectite, negatively impacting shale porosity. Siliceous shale undergoes carbonate cementation and quartz dissolution, contributing to increased porosity, particularly in mesopores. Calcareous shale experiences diagenesis characterised by carbonate formation and dissolution, with a prevalence of siderite. In carbonate, clay, and silt-bearing shale, the dissolution of K-feldspar contributes to illitization of kaolinite. Argillaceous shale, characterised by more clay minerals and lower mesopore volume, is identified as a potential hydrocarbon seal. Siliceous shale, with the highest pore volume and abundant inter-mineral pores, emerges as a promising shale oil reservoir. These findings contribute to a comprehensive understanding of shale properties, aiding in the prediction of shale oil exploration potential in the studied area.

1. Introduction

Shale has attracted much more attention in the worldwide as the energy demand highly increased in the past years. Shale oil refers to thermally matured oil that has been generated from organic matter and stored in host shales or migrated to adjacent intervals (Jarvie, 2012; Zou et al., 2013). Since 2007, the United States has been exploring for shale oil, and the discovery of shale oil in the Eagle Ford and Permian Basin shale formations in 2011 resulted in much increased production (Maugeri, 2013). China has a large potential for shale oil resources, which were estimated to be around 3700 × 10^8 tons in the major continental basins in China (Yang et al., 2019). The geographical surface area of shale oil in China was estimated to be around 8.5 × 10^4 km^2 (Hu et al., 2020). Compared to source rocks in North America, however, most shale oil source rocks in China have lower thermal maturity and lower total organic carbon contents, higher wax contents, greater lateral distributions and lower thicknesses (Zhao et al., 2020). Therefore, the exploration and development of shale oil in China presents many challenges. Lacustrine shale is regarded as an important source rock for shale oil. Compared to marine shale, lacustrine shale has more complex lithologies and higher heterogeneity as it has multiple terrestrial sources and is sensitive to environmental changes (Ma et al., 2016, 2017; Teng et al., 2021; Xu et al., 2021; Wang et al., 2022). Previous studies have studied the organic matter sources, depositional environment, lithologies, pore structure and geochemical characteristics of lacustrine shale (Zhang et al., 2017; Chen et al., 2019; Guo et al., 2022; Liu et al., 2022a, 2022b; Yang et al., 2023). Organic matter of lacustrine shale is dominated by Type I and II (Wang et al., 2019). Pores are categorised into three

* Corresponding author.
** Corresponding author.
E-mail addresses: baibin81@petrochina.com.cn (B. Bai), wang_jp@jlu.edu.cn (J.-P. Wang).

https://doi.org/10.1016/j.petsci.2023.12.024

types: organic matter-hosted pores, framework minerals-associated pores and clay minerals-associated pores (Chen et al., 2019). The pore size of lacustrine shale is larger than marine shale (Chen et al., 2019; Ma et al., 2018, 2019). The studies of diagenetic history of lacustrine shale are relatively few. Liu et al. (2022) investigated the diagenetic sequence of the lacustrine shale from the Qingshankou Formation in the Songliao Basin and linked it to the thermal maturation processes of shale. Yang et al. (2023) described the diagenesis of tuffs in lacustrine shale from the Ordos Basin, including the dissolution of plagioclase, illitization of smectite and carbonate cementation.

The Ordos Basin is a large intracratonic basin in China, which contains up to 10×10^8 metric tons of oil from Mesozoic reservoirs (Duan et al., 2008). There are 10 units in the Yanchang Formation, named Chang 10 Member to Chang 1 Member from oldest to youngest. The Chang 7 Member has been recognised as a high-quality source rock (Duan et al., 2008, 2013). However, the Chang 7 source rock as a reservoir possesses complex pore networks, low porosity and permeability and variable amounts of fractures (Hua et al., 2017; Yang et al., 2016). Shale oil in the Chang 7 Member is mainly stored in nano pores in non-marine shales (Zou et al., 2013). Mineral composition and distribution play an important role in establishing the pore systems in shales (Ross and Bustin, 2009; Franks and Zwingmann, 2010; Chen et al., 2016; Schwartz et al., 2019; Wang et al., 2021a, 2021b). Diagenetic processes can lead to complex alterations of shale porosity and permeability, and therefore needs to be assessed as part of exploration and production plans for shale oil (Milliken et al., 2012; Liang et al., 2018; Liu et al., 2019; Hao et al., 2021, 2023). However, less work has been done on the detailed studies of mineralogical development and diagenetic sequence of lacustrine shale from the Ordos Basin. This study utilizes the lacustrine shales from the Y56, L231 and Ly10 wells from the oil-bearing Chang 7 Member, Yanchang Formation, Ordos Basin as examples to illustrate the mineralogical development and diagenetic alteration of different lithofacies in lacustrine shale. This study links diagenetic development of minerals closely to different lithofacies and the control factors on the pore distribution, which helps us better predict the potential 'sweet spots' for shale oil production in the Ordos Basin.

2. Geological setting

The Ordos Basin is located in northwestern China and developed on the North China Platform (Zhang et al., 1998). It consists of six structural units: Western Edge Thrusting Belt, Tianhuan Depression, Yishan Ramp, Jinxi Flexural Fold Belt, Yimeng Uplift and Weibei Uplift (Fig. 1). The Ordos Basin plunges from northwest to southeast (Ji et al., 2010). The Ordos Basin was formed during the Indosinian movement in the Late Triassic (Zhang et al., 1997). Its evolution dates from the Pre-Cambrian and experienced three stages of evolution (Fig. 1): (i) a Cambrian–Early Ordovician marine deposition stage, (ii) a Middle Ordovician–Middle Triassic marine and terrestrial alternation stage, and (iii) a Late Triassic–Early Cretaceous terrestrial deposition stage (Chinese Petroleum Geology Editorial Committee (CPGEC), 1992). A marine environment prevailed from the Permian to Middle Triassic until regional uplift caused the withdrawal of sea water and the deposition of terrestrial deposits during the Late Triassic (Johnson et al., 1989). There are two hydrocarbon systems present in the basin: a Paleozoic gas and a Mesozoic oil system (Yang et al., 2005).

The Yanchang Formation comprises fluvial-clastic rocks, namely sandstones, siltstones, shales and tuff intervals, which is up to 1000 m in thickness in the northern part of basin and 1400 m in the southern part of basin (Ji et al., 2010; Qiu et al., 2014). During the deposition of the Chang 7 Member, the basin experienced intensive tectonic thinning subsidence. A semi-deep to deep-lacustrine shale was deposited during that period (Bai and Ma, 2020).

3. Methods

The core samples were collected from Y56, L231 and Ly10 wells. A continuous sampling carried out at 50 cm intervals in each well. Analyses include X-ray fluorescence (XRF), Rock-Eval (R_o), total organic carbon (TOC), rock pyrolysis, gas adsorption, mercury injection reservoir tests and trace element were conducted. Petrographic and mineralogical analysis was performed to identify minerals, determine the distribution of minerals and lithofacies features in the studied samples using a Zeiss optical microscope, a scanning electron microscope (SEM), and a Bruker D8 Advance X-ray Diffractometer (XRD) at the State Key Laboratory of Nuclear Resources and Environment at the East China University of Technology. The SEM analysis was conducted with a voltage setting of 5 kV and a current of 0.4 nA. XRD analysis was performed under the conditions of 35 kV and 15 mA. The total carbon content (TOC), organic carbon and sample maturity were determined to evaluate the evolution of organic matter. Vitrinite reflectance measurement was conducted using MSP200 equipment at the Key Laboratory of Exploration Technologies for Oil and Gas Resources, Ministry of Education, Yangtze University. R_o and TOC analysis were performed using CS-I and Vinci Technologies equipment at the Key Laboratory of Petroleum Geochemistry, China National Petroleum Corporation. Porosity was measured using nitrogen adsorption and mercury injection experiments to investigate the pore network development at the Beijing Centre for Physical & Chemical Analysis, which can obtain pore size distribution and pore volume and specific surface area parameters. The nitrogen adsorption experiment used ASAP 2460 and tested at −196 °C (77 K). The mercury injection instrument was AutoPore IV 9520 with a maximum inlet pressure of 3000 psi. Furthermore, some SEM photomicrographs were processed using ImageJ to show different pore types. The elemental composition was determined. The analysis of major elements was carried out using an AxiosmAX XRF spectrometer at the Beijing Research Institute of Uranium Geology. Trace element analysis was performed using an Element XR Inductively coupled plasma mass spectrometry (ICP-MS).

4. Results

4.1. Mineralogical composition in Ordos shales

Whole rock XRD analysis shows that the studied samples are mainly composed of quartz (4–69%), K-feldspar (≤12%), plagioclase (≤21%), calcite (≤32%), dolomite (≤14%), siderite (≤43%), ankerite (≤37%), pyrite (≤37%) and clay minerals (6–92%). Clay minerals are dominated by illite/smectite mixed-layer minerals (I/S). I/S accounts for 30–95% of the total clay minerals, followed by illite (7–60%), kaolinite (1–55%) and chlorite (1–16%). Based on their mineralogical composition, the studied samples can be divided into eight microfacies (Gamero-Diaz et al., 2012): i) Facies 1, argillaceous siliceous shale; ii) Facies 2, clay-rich siliceous shale; iii) Facies 3, mixed shale; iv) Facies 4, silica-rich argillaceous shale; v) Facies 5, mixed carbonate shale; vi) Facies 6, carbonate siliceous shale; vii) Facies 7, mixed siliceous shale and vii) Facies 8, silica-dominated shale (Fig. 2).

4.2. Textural observations and mineralogical development

Based on their sedimentological characterisation and sample textures, they can be further classified into four microfacies associated types: i) argillaceous shale (Facies 4); ii) siliceous shale

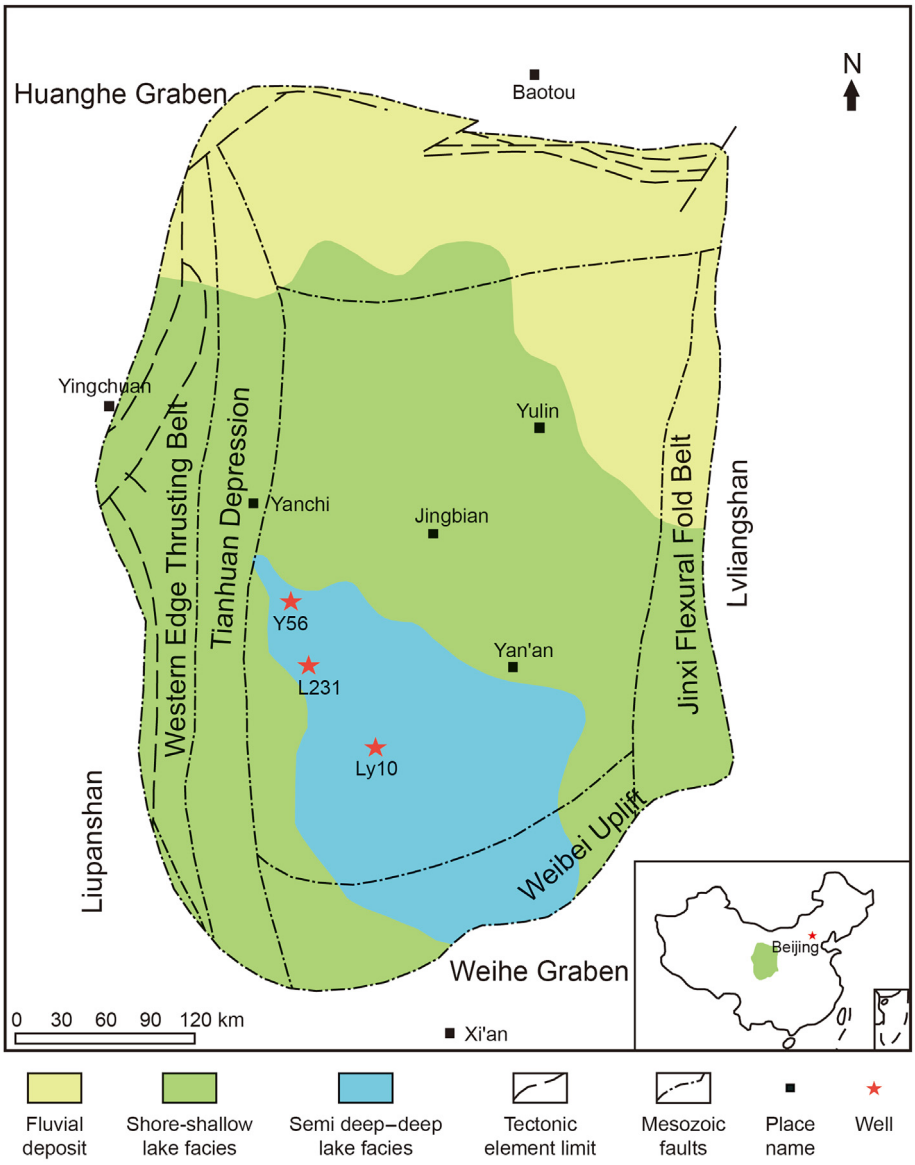

Fig. 1. Tectonic location and sedimentary facies plane distribution of the Ordos Basin.

(Facies 2, 7 and 8); iii) calcareous shale (Facies 5) and iv) carbonate, clay and silt-bearing shale (Facies 1, 3 and 6) (Fig. 2). The total organic content (TOC) of argillaceous shale is up to 5.0%. Calcareous shale contains the lowest average TOC value (1.3%). The average TOC value of siliceous shale is 3.7%. The TOC value of carbonate, clay and silt-bearing shale is up to 10.5%, with the average value of 4.3%. The T_{max} data of the studied sample is in the range of 407–450 °C. Based on the equation ($Vitrinite_{eq} = 0.018\,T_{max} - 7.16$) (Jarvie et al., 2001), the equivalent vitrinite reflectance of the studied samples is in the range of 0.17–0.94. Y56-131 has the lowest Vr_{eq} ($Vitrinite_{eq}$) value of 0.17. Excluding Y56-131, the average Vr_{eq} of the studied samples is 0.79. The average Vr_{eq} values of argillaceous, siliceous, calcareous shale are 0.82, 0.82 and 0.89, respectively. The Vr_{eq} of carbonate, clay and silt-bearing shale is 0.76.

4.2.1. Argillaceous shale

4.2.1.1. Facies 4 silica-rich argillaceous shale. The succession between 3025 and 3052 m is dominated by argillaceous shales (Facies 4) consisting of a clay matrix (50–75%), silt-sized quartz (25–50%) and minor carbonate minerals (0–10%). Weak silt-rich laminations are present (Fig. 3), but generally the facies is structureless. Silt

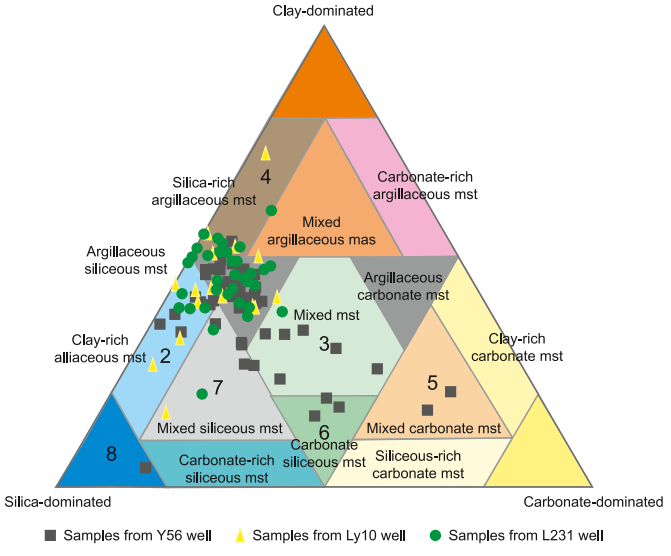

Fig. 2. Mineral composition triangles of the eight identified sedimentary microfacies in Ordos shales, modified after Gamero-Diaz et al. (2012).

grains are sub-rounded with the size lower than 10 μm (Fig. 3). In the μm- and nm-scale, organic matter is disseminated in the matrix and some irregular pores are present around silicates (Fig. 3). Clay matrix is dominated by I/S, illite and kaolinite (Fig. 3).

4.2.2. Siliceous shale

Siliceous shales consist of Facies 2, 7 and 8. They are characterised by high quartz and feldspar (50–74%), moderate clay contents (6–42%) and carbonate minerals (1–26%). They are distributed through the whole core.

4.2.2.1. Facies 2 clay-rich siliceous shale. This facies was either deposited as structureless beds. Some large grains of quartz are present and weakly aligned, suggesting some preferential bedding (Fig. 3). Clay minerals can be observed in μm-scale and nm-scale. Pores were found around silicates (Fig. 3). Quartz overgrowth on detrital quartz was observed in this facies. Compared to silica-rich argillaceous shales (Facies 4), this facies contains much more detrital quartz and quartz overgrowth (Fig. 3).

4.2.2.2. Facies 7 mixed siliceous shale. In Facies 7, laminations are abundant and show current ripples, organised into fining upwards beds less than 1 mm thick. These beds have erosive bases, and clay-rich and organic-matter rich tops. Lenticular fabric was observed with the maximum length up to 6 mm, which is composed of silt-grains (Fig. 3). Quartz grains are present in the matrix (Fig. 3). In the μm-scale, samples contain organic matter and inter-mineral pores. Ankerite occurs in this shale type and was precipitated within the broken muscovite planes (Fig. 3).

4.2.2.3. Facies 8 silica-dominated shale. This facies is characterised by abundant quartz content with minor clay mineral and carbonate

Microfacies associations	Microfacies	mm-scale	μm-scale	nm-scale	Features	Diagenetic minerals	Diagenetic description
Argillaceous mudstone	Facies 4 Silica-rich argillaceous mudstone	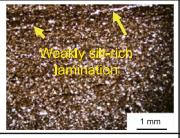	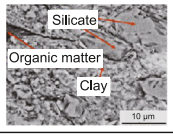	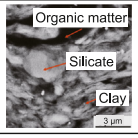	Structureless or weakly silt-rich laminations. Large organic particles and some irregular pores can be observed.	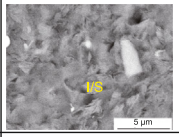	Diagenetic minerals are dominated by I/S mixed layer, illite and kaolinite
Siliceous mudstone	Facies 2 Clay-rich siliceous mudstone	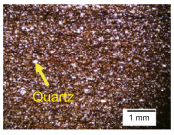	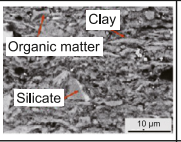	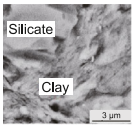	Structureless beds, with bioturbated structure.	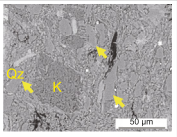	Kaolinite, I/S mixed layer, pyrite, illite, quartz overgrowth (yellow arrows)
	Facies 7 Mixed siliceous mudstone	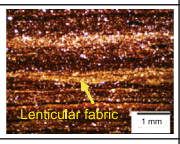	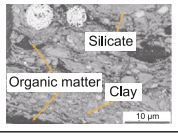	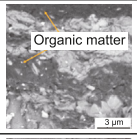	Abundant laminations with fining upwards beds less than 1 mm thick. Large organic matter belt can be observed in the matrix.	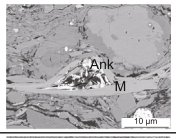	Pyrite, ankerite, broken organism tests and muscovite due to deformation and compaction
	Facies 8 Silica-dominated mudstone	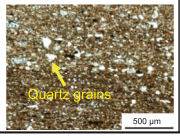	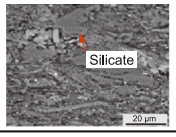	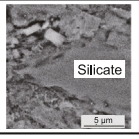	Laminations are rarely observed, with high bioturbation.	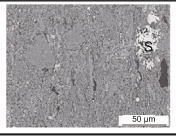	Quartz overgrowth, siderite, chlorite

Microfacies associations	Microfacies	mm-scale	μm-scale	nm-scale	Features	Diagenetic minerals	Diagenetic description
Calcareous mudstone	Facies 5 Mixed carbonate mudstone	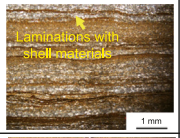	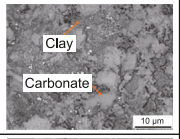	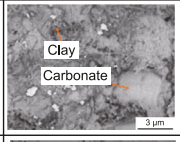	Thin-bedded laminations (<0.5 mm) with fining upward grain sizes.	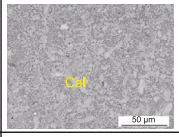	Dominated by calcite
Carbonate, clay and silt-bearing mudstone	Facies 1 Argillaceous siliceous mudstone	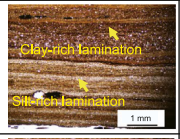	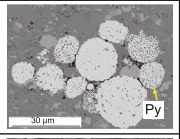	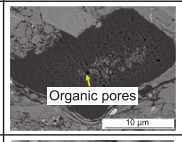	Thin bedded laminations of silt-clay (<1 mm), with fining-upward textures.	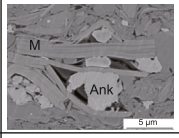	Ankerite precipitated in muscovite planes
	Facies 3 Mixed mudstone	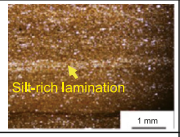	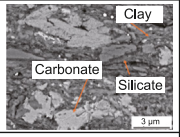	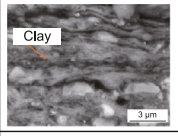	Silt-laminations within clay-dominated matrix, and bioturbation.	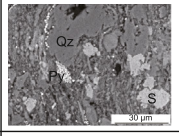	Pyrite are common and siderite are present
	Facies 6 Carbonate siliceous mudstone	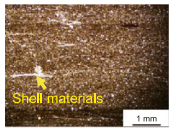	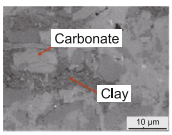	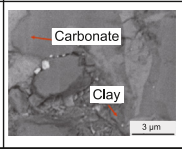	Laminations are not common with rare finer, clay-rich laminations locally.	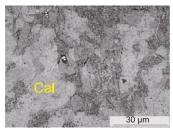	Carbonate minerals are common

Fig. 3. Multi-scale characterisation of the eight facies identified in the selected samples. I/S: illite/smectite mixed-layers; Cal: calcite; M: muscovite; Ank: ankerite; Qz: quartz; S: siderite; Py: pyrite; K: kaolinite.

contents. TOC is moderate (up to 4.6%). Laminations are rarely observed, but some samples consist of faint, poorly developed fabrics (Fig. 3). In the μm-to nm-scale, pores are present around silicates (e.g. quartz and feldspar grains). Siderite is present (Fig. 3).

4.2.3. Calcareous shale

Calcareous shale mainly accumulated in the upper unit of the core above the depth of 3015 m. This type is dominated by Facies 5. Some samples (i.e. sample 173) shows some weak laminations (Fig. 3). Laminations such as thin beds (<0.5 mm) are common in some samples (i.e. Y56-171). These laminations are mainly composed of shell materials (Fig. 3). These beds display a fining-upward grain size and have slightly erosive bases as well as clay-rich tops (Fig. 3). Calcite is the main cement in this facies (Fig. 3). Pores are not common.

4.2.4. Carbonate, clay and silt-bearing shale

This facies associate is the main type of Ordos shales, including microfacies 1, 3 and 6. The laminations can be thin-bedded, weakly disturbed or even no present. The TOC content is found to be relevant to the development of laminations.

4.2.4.1. Facies 1 argillaceous siliceous shale. This facies is characterised by high quartz (25–50%) and clay contents (25–50%) with minor amounts of carbonate minerals (0–25%). TOC values are high, up to 9.0%. Laminations of silt-clay are present in some samples, although absent in others (Fig. 3). Where lamination is present it tales for the form of both planar and current ripple lamination (Fig. 3). These laminations stack into thin (<1 mm) beds, which display fining-upward textures (Fig. 3). Beds display erosive bases in places and are capped by clay-rich laminae. Aggregates of pyrite are more abundant in this facies (Fig. 3). Intra-mineral pores are present within pyrite. Organic pores were observed in this facies in the nm-scale (Fig. 3).

4.2.4.2. Facies 3 mixed shale. This facies is characterised by similar amounts of quartz, clay and carbonate minerals. There are moderate to high TOC values (up to 8.1%). Laminations are present in some parts of this facies and take the form of silt-laminations within clay-dominated matrix (Fig. 3). Bioturbation is present in places. Siderite is present in this facies and takes the euhedral form.

4.2.4.3. Facies 6 carbonate siliceous shale. This facies is characterized by abundant carbonate minerals (25–50%), with moderate quartz (10–40%) and clay mineral contents (10–40%). TOC is low (up to 3.28%). Laminations are uncommon (Fig. 3), but where present take the form of finer laminations of clay-rich deposits, suggesting that currents were variable. Calcite is the main cement in this facies (Fig. 3).

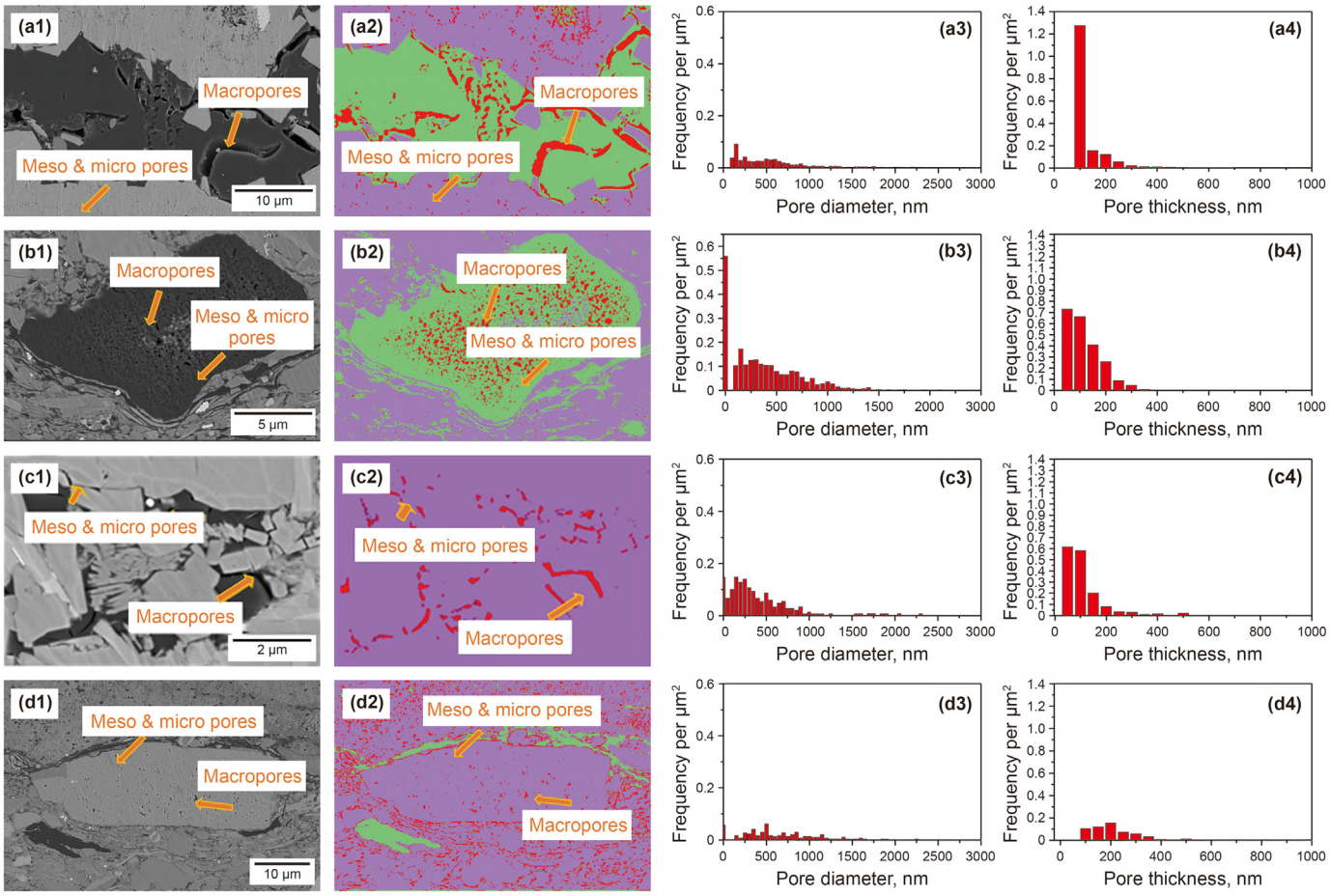

Fig. 4. Different types of pores and pore size in the studied samples. Rows: **(a)** Cracked pores in organic matter. **(b)** Spongy pores in organic matter. **(c)** Pores in matrix (inter-mineral pores). **(d)** Pores inside minerals (intra-mineral pores). Columns: (1) SEM images. (2) Segmented images. Purple-minerals, green-organic matter, red-pores. (3) Pore diameter distribution. (4) Pore thickness distribution.

4.3. Pore types

Based on the SEM photomicrographs, pores in the studied samples can be distinguished as i) cracks within organic matter, ii) intra- organic pores, iii) inter-mineral pores and iv) intra-mineral pores (Fig. 4).

Some cracks were identified within certain types of organic matter (Fig. 4(a)). Some of them distribute between organic matter and minerals while the others are purely within organic matter. These cracks are long and thin but the equivalent diameters are relatively large.

Intra-organic matter pores are commonly distributed in other types of organic matter (Fig. 4(b)). They are sphere in geometry and spongy in distribution. They can be as big as 300 nm or smaller than 1 nm. The thickness and the equivalent diameter are similar in sizes.

Inter-minerals pores/voids commonly occur around silicates and muscovite planes (Fig. 4(c)). They are preferred to be wedge-shape or irregular shapes and were formed owing to the compaction. The thickness is slightly larger than diameter. The voids between muscovite planes provide the space for the precipitation of carbonate minerals (e.g., siderite and ankerite).

Intra-mineral pores are present within calcite and feldspar (Fig. 4(d)), indicating the dissolution of these minerals. These pores are dominated by polygon-shape with similar sizes in thickness and equivalent diameter.

4.4. Pore size distribution

The distribution of pore diameter and surface area in the different types of shale is shown in Fig. 5. The pore width in all samples mainly displays two peaks with the pore diameters ranging from 25 to 50 nm and from 65 to 135 nm, respectively. Hence, the pore types in shale of the Yanchang Formation are mainly dominated by mesopores and macropores. Intra- organic pores include macropores and mesopores. Inter-mineral pores are dominated by macropores. Intra-mineral pores are dominated by mesopores and micropores and less macropores. Fig. 5 shows that micropores and mesopores contribute more to the surface area than macropores. Although pores in the studied samples are dominated by intra- organic pores and inter-mineral pores, the role of intra-mineral pores cannot be neglected. The total pore volume

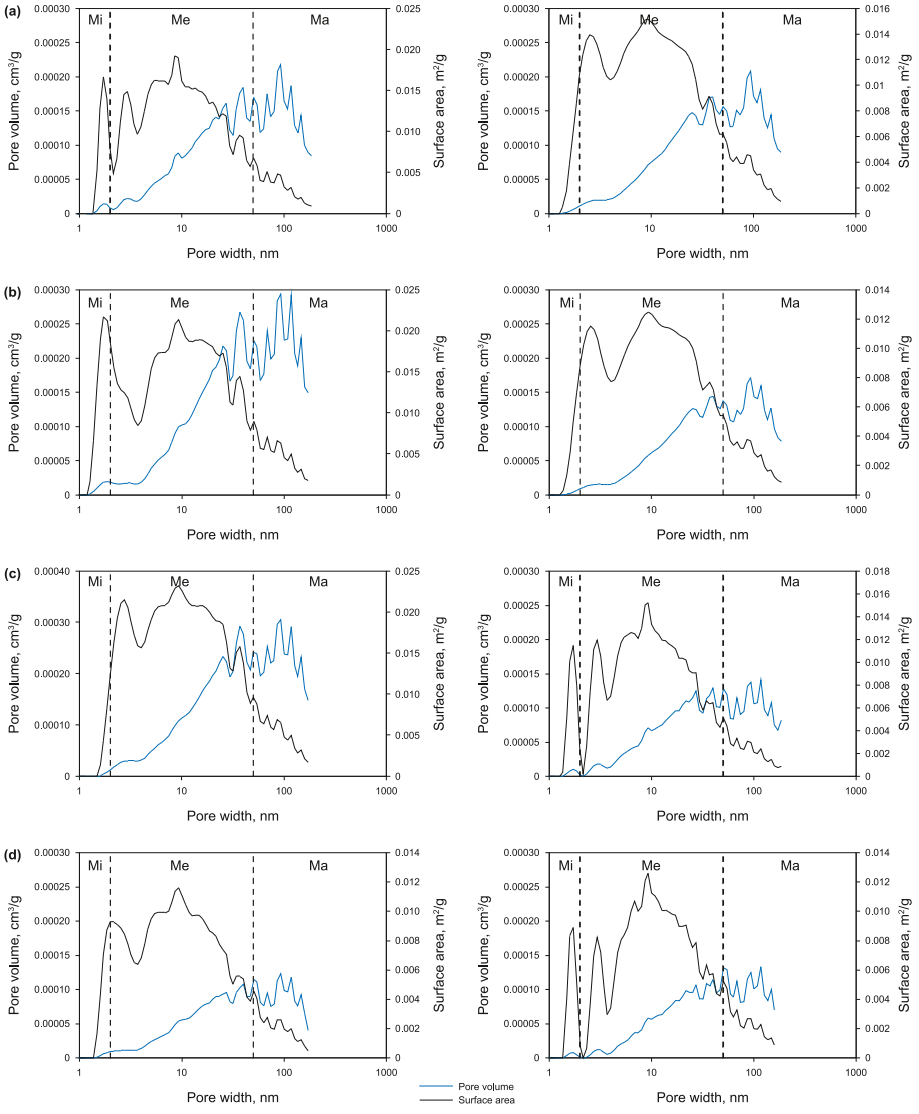

Fig. 5. The distribution of pore volume and surface area in the studied samples from Yanchang Formation. Mi: micropores; Me: mesopores; Ma: macropores. **(a)** Argillaceous shales. **(b)** Siliceous shales. **(c)** Calcareous shales. **(d)** Carbonate, clay and silt-bearing shales.

of argillaceous, siliceous, calcareous and carbonate, clay and silt-bearing shale is 0.0061, 0.0082, 0.0045 and 0.0039 cm^3/g (Fig. 5). This indicates that siliceous shales contain more pores than the other three shale types.

4.5. Elemental analysis

The major elements analysis shows that the studied samples are dominated by Si and Al, with the values ranging from 26% to 64.5% and ranging from 9% to 20%, respectively. CaO and MgO are enriched in calcareous shale and the value of CaO is up to 20.5%.

Trace elements can be used to indicate paleo-environment for the deposition of shale. Redox-sensitive elements Cr, Mo, Ni and V as well as their ratios were detected and calculated. The Ti/Al can be used as proxy for sedimentation rate and a higher Ti/Al value indicates a higher sedimentation rate (Peng et al., 2021, 2023). The Ti/Al values of studied samples range from 0.028 to 0.046. The value of V/(V + Ni) ranges from 0.58 to 0.91. The value of Sr/Ba ratio can be used as an indicator for salinity, which is in the range of 0.23–0.75.

4.6. Diagenetic processes

Integrating the XRD and SEM data, diagenetic minerals in this study include: pyrite, calcite, dolomite, ankerite, siderite, quartz, kaolinite, illite and illite/smectite mixed-layers. Diagenetic alterations consist of physical compaction, cementation of diagenetic minerals (e.g., carbonates and quartz), dissolution of calcite and quartz, replacement of feldspar by kaolinite and transformation from smectite to illite.

4.6.1. Compaction

Compaction occurred soon after the deposition of sediments. Pore water would have been released during compaction. Organic matter is aligned parallel to the bedding planes (Fig. 6(a)). Some shell material and mineral grains have broken (Fig. 6(b)). Deformation structures were found around broken shell material (Fig. 6(c) and (d)). Compaction increases as overburden strata increases. The relationship between quartz grains is mainly of line contact (Fig. 6(e) and (f)).

4.6.2. Pyrite

Pyrite is present in most of the studied samples. It is generally in the form of framboidal and euhedral pyrite, which is disseminated through samples. They are also present within voids. Framboidal pyrite is mostly spherical and closely packed with microcrystals of 0.5–1 μm in diameter (Fig. 7(a)). The fabric surrounding this type of pyrite was deformed (Fig. 7(a) and (b)), indicating that the compaction occurred after the formation of framboidal pyrite. Some microcrystals of framboidal pyrite were also disseminated in the matrix (Fig. 7(b)). Euhedral pyrite is also present and sometimes occurs as aggregates within the intraskeletal porosity (Fig. 7(c) and (d)).

4.6.3. Calcite

Calcite is present throughout the studied samples and associated with other minerals (Fig. 8(a)–(f)). It is the main cement in calcareous mudstone and also common in carbonate, clay and silt-bearing mudstone. It can be divided into two types. Macrocrystalline calcite with the size over 10 μm has irregular shapes (Fig. 8(b)–(e)). They enclose the quartz in some cases (Fig. 8(e)). Micro-crystalline calcite cements are 1–5 μm in diameter. They were formed around quartz cements and overgrowth (Fig. 8(c)). They are disseminated in the clay matrix and enveloped by illite and I/S mixed layer clay minerals (Fig. 8(d)). Hence, they formed before the clay transformation in carbonate, clay and silt-bearing mudstone.

4.6.4. Dolomite, ankerite and siderite

They are also common cements in carbonate, clay and silt-bearing mudstone. Dolomite has a rhombohedral habit and is surrounded by ankerite (Fig. 9(a) and (b)). The dolomite and its ankerite rims were formed relatively early. Siderite is present in some samples with irregular shape around quartz (Fig. 9(c)). Siderite replaced I/S mixed layer clay minerals as well, however, it was surrounded by the illite (Fig. 9(d)).

4.6.5. Quartz

Authigenic quartz mainly takes the form of quartz overgrowth in the studied samples. Quartz overgrowth is present with detrital quartz. This is the common cement in siliceous mudstone. The crystal termination is clear on quartz grains, and thus it is clear to observe the overgrowth of quartz around detrital quartz (Fig. 10(a)). Quartz overgrowths are closely linked with the illitization of smectite and kaolinite. Sometimes clay minerals surround the quartz grains and its overgrowth (Fig. 10(b)). Micro-sized quartz is common in carbonate, clay and silt-bearing shales. Compared to detrital quartz grains, they are small, usually 1–5 μm in diameter (Fig. 10(c)). In high magnification photographs, the outline of micro-sized quartz is clear (Fig. 10(c)). There is no quartz overgrowth around it. Some evidence about the dissolution of primary micro-sized quartz at grains contact was found in this study. As shown in Fig. 10(d), micro-sized quartz dissolved from the edge and recrystallized quartz penetrated into primary micro-sized quartz grains. This is a result of pressure dissolution of quartz during burial diagenesis. Moreover, the replacement of micro-sized quartz by siderite was also observed (e.g., in Y56-214; Fig. 10(d)).

4.6.6. Clay mineral transformation

Based on the SEM and XRD data, the clay minerals include kaolinite, illite, illite/smectite (I/S) and chlorite. Clay formation and transformation are main diagenetic processes in argillaceous mudstone.

4.6.6.1. Kaolinite and illitization of kaolinite. The proportion of kaolinite in the clay minerals is in the range of 1–55% for all samples. The illitization of kaolinite was found in the studied samples. Kaolinite cements were formed in the matrix. Illite was formed along the cleavage planes of kaolinite and replaced some part of kaolinite (Fig. 11(a)). The reaction is shown below. Moreover, illite was formed along the kaolinite (Fig. 11(b)). Overall, kaolinite cements were formed first and replaced the detrital feldspar during the early stage of diagenesis. The illitization of kaolinite occurred in the late stage of diagenesis with the presence of source of potassium:

$$Al_2Si_2O_5(OH)_4\,(\text{kaolinite}) + KAlSi_3O_8\,(\text{K-feldspar}) = KAlSi_3O_{10}(OH)_2\,(\text{illite}) + 2SiO_2\,(\text{quartz}) + H_2O$$

4.6.6.2. Illite and illitization of smectite. Authigenic illite occurs commonly as a clay cement in the studied samples, especially argillaceous mudstone. Illite occupies 7–27% and illite/smectite mixed-layer minerals account 30–74% of the total content of clay minerals. Except for sample Y56-76, clay minerals in all samples are dominated by illite/smectite mixed-layer clay minerals. The

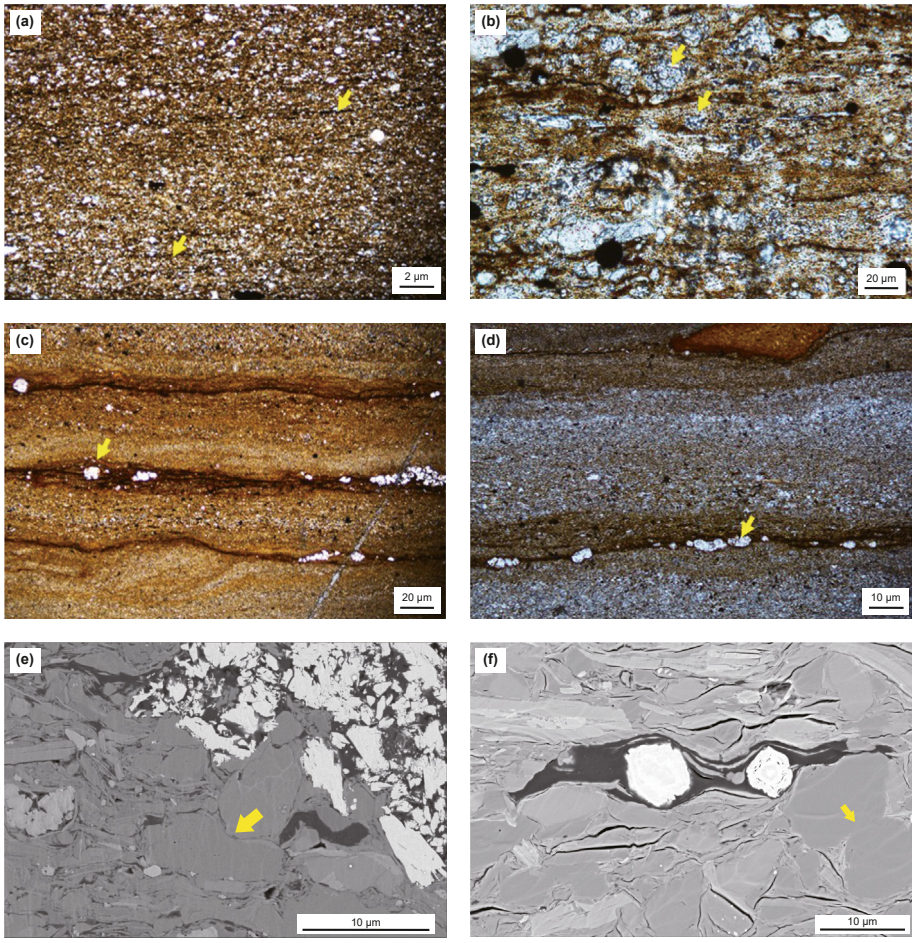

Fig. 6. Textures resulting from post-depositional compaction. **(a)** Organic matter (yellow arrows) aligned parallel to the bedding planes, Y56-53. **(b)** Broken shell material and mineral grains, Y56-157. **(c)** Deformation structure around shell material, Y56-163. **(d)** The broken shell material and their surrounding deformation structures, Y56-180. **(e, f)** The line contact between two minerals, Y56-07 and Ly10-19.

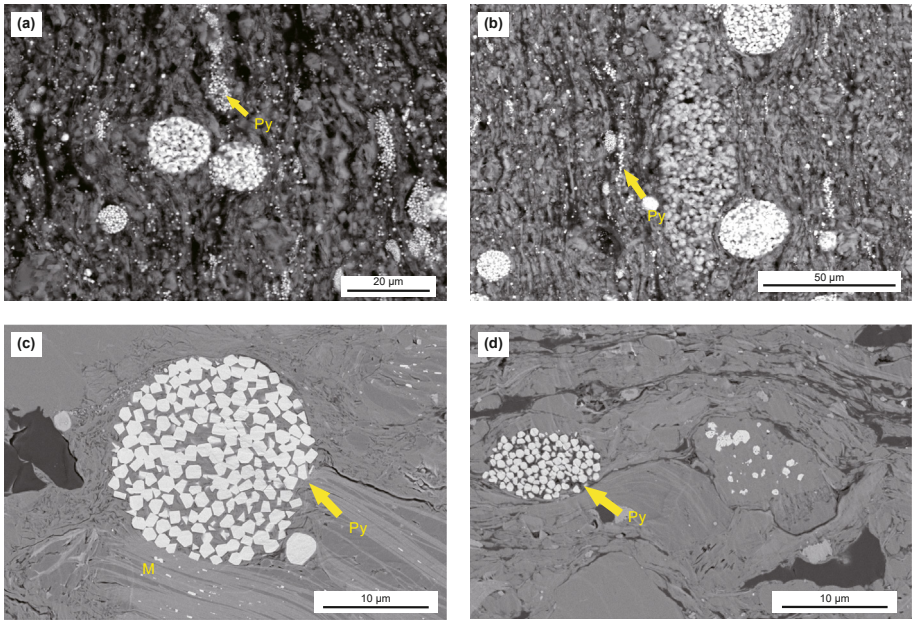

Fig. 7. Framboidal pyrite in the studied samples. **(a)** Closely packed framboidal pyrite. The surrounding structure has been deformed, L231-46. **(b)** Framboidal pyrite and aggregates. Framboidal pyrite was precipitated along fractures in some cases, L231-48. **(c)** High resolution image of euhedral pyrite, Y56-72. **(d)** Euhedral pyrite within the intraskeletal porosity, Y56-66. Py: pyrite; M: muscovite.

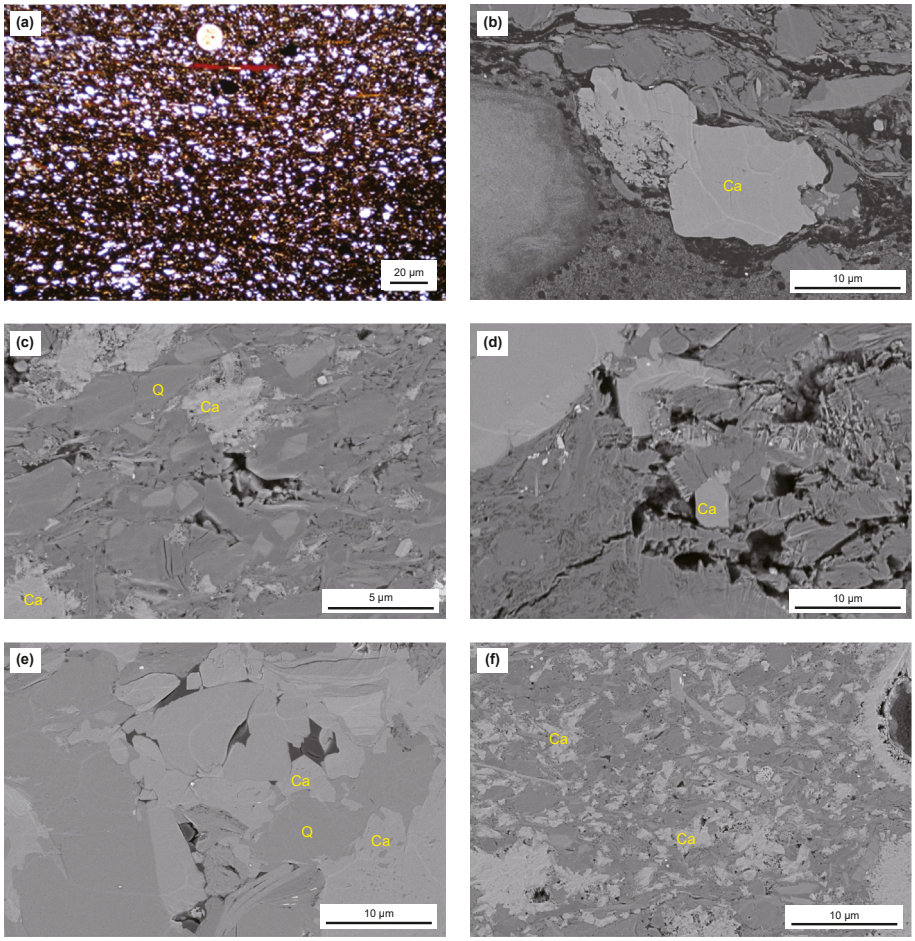

Fig. 8. Calcite cements in the studied samples. **(a)** Disseminated carbonates in the studied samples, Y56-187. **(b)** Macro-crystalline calcite in the matrix associated with organic matter. **(c)** Micro-crystalline calcite cements around the quartz grain, Y56-04. **(d)** Micro-crystalline calcite crystals in the clay matrix enveloped by I/S mixed-layer clay minerals, Y56-13. **(e)** Macro-crystalline calcite cements in the matrix, enclosing quartz cement, Y56-03. **(f)** Calcite cements in the Ordos shale, Y56-205. Ca: calcite; Q: quartz.

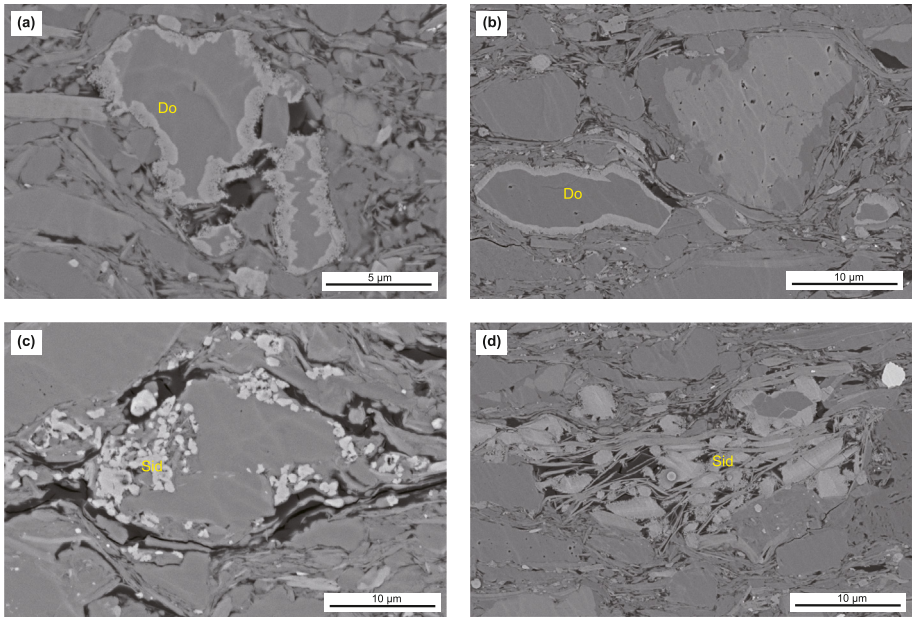

Fig. 9. Dolomite, ankerite and siderite in the studied samples. **(a)** Non-ferroan dolomite with a rhombohedral habit, surrounded by ankerite at the rim, Y56-101. **(b)** Non-ferroan dolomite with the ankerite rim, Y56-199. **(c)** Siderite cements in the studied samples, Y56-157. **(d)** Siderite cements in the studied samples, replacing the I/S mixed-layer clay minerals and surrounded by illite, Y56-157. Do: dolomite; Sid: siderite.

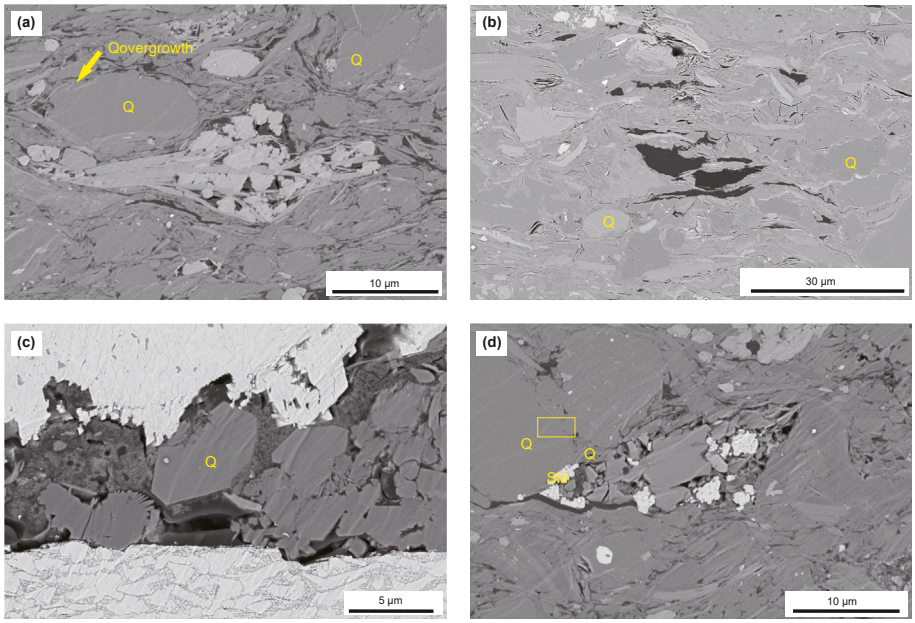

Fig. 10. Micro-sized quartz and its overgrowth in the studied samples. **(a)** Detrital quartz and quartz overgrowth, Y56-37. **(b)** Quartz cements and clay minerals, Ly10-10. **(c)** Micro-sized quartz crystals in the matrix, Y56-53. **(d)** The replacement of micro-sized quartz grains by siderite cements and the dissolution of quartz at grain contacts. The squares show that the pits on the primary micro-sized quartz and the newly grown recrystallized quartz, Y56-214. Q: quartz; Sid: siderite.

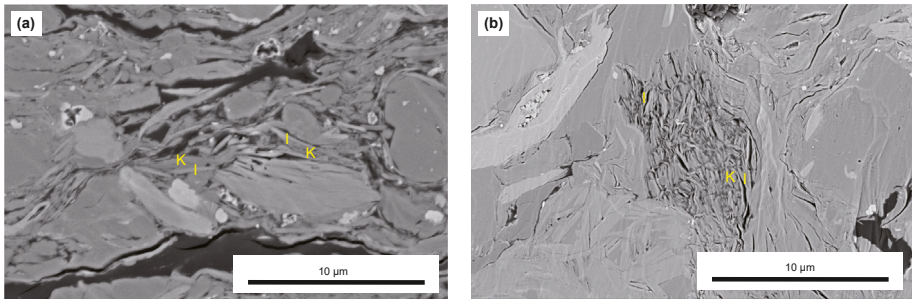

Fig. 11. Kaolinite cements in the studied samples. **(a)** The replacement of kaolinite by illite, Y56-27. **(b)** Kaolinite cements surrounding by illite, Ly10-16.

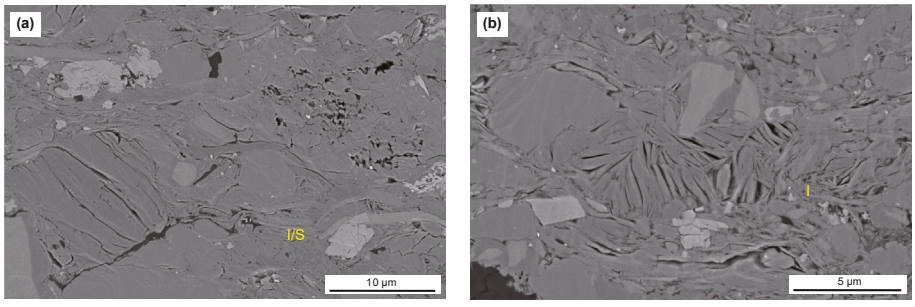

Fig. 12. Illite and illite/smectite mixed-layer clay minerals in the studied samples. **(a)** Illite/Smectite mixed-layer clay minerals in the matrix, Y56-157. **(b)** Hairy illite, Y56-163.

illitization of smectite is a common mineral reaction during the burial diagenesis of shales. Based on the XRD data, the ratio of illite/smectite mixed-layer clay minerals to illite in the studied samples ranges from 2 to 6. The average of this ratio is 3, indicating that the transformation degree from smectite to illite is moderate. The illite/smectite was found around other minerals such as quartz and calcite cements (Fig. 12(a)). In deeper burial diagenesis, the alteration of smectite to illite can release Si to porewaters. The illite in the studied samples almost has a hairy habit and has been crystallised (Fig. 12(b)).

5. Discussion

5.1. Depositional environment

Based on the detailed petrographic, mineralogical and geochemical analysis, the studied samples are used as examples to elucidate the depositional and diagenetic controls on four types of

shales and discuss their potential on finding the 'sweet spot' of shale oil.

Firstly, the argillaceous shales show weak silt-rich laminations and much more clay minerals than other types of shales (Fig. 3). The deposition of abundant clays is a result of suspension fall out settling (Könitzer et al., 2014). The input of the relatively rare silt-grains into argillaceous shales was likely a result of density flows, which can also be observed in marine shale (Newport et al., 2018). This facies was hence deposited in a deep-lake environment with a low sedimentation rate (Fig. 13(a)–(c)). The pores in this facies are dominated by intra-mineral pores in mixed layer of clay minerals. The transformation of clay minerals can reduce the porosity and permeability of shale (Mondol et al., 2007; Mondol, 2009). Hence, this facies is a potential seal for shale oil reservoirs.

The siliceous shales contain more quartz and feldspar, with the dominant source being detrital. These silt grains were likely transported by river into the lake (Fig. 13(a)–(c)) (Lazar et al., 2015). Lenticular laminations can be observed in the samples, suggesting a weakly hydrodynamic environment with low density turbidity or undercurrent developing when they formed (Peng, 2021; Peng et al., 2022). This facies was likely accumulated at the semi-deep lake (Fig. 13(b) and (c)). Organism tests can be seen in this facies (e.g., Facies 7), indicating that the bioturbation may occur and destroy some original fabrics. Pyrite is common in this facies and iron-bearing minerals were observed as well. This indicates that the early diagenetic environment was ferruginous (Yuan et al., 2021). Bioturbation reworked shales and may increase the porosity and permeability of shales by creating fluid pathway and burrows (Gingras et al., 2015), possibly contributing to the formation of some fractures. This facies contains many inter-mineral pores between silicates with the highest pore volume. It is a potential reservoir for shale oil.

The calcareous shales contain shell material and wavy laminations. Carbonates include shell materials, calcite, dolomite and ankerite. Low to moderate TOC contents in this facies suggest low productivity in the basin at these times, or low preservation. The origins of dolomite in this facies are speculated. Lin et al. (2019) suggested that dolomite was formed in a relatively high salinity, high temperature and high pH of the water column. However, the values of Sr/Ba ratios indicate that the studied samples were deposited in water with low salinity consistent with fresh to brackish water (He et al., 2019; Wei and Algeo, 2020). Zhang et al. (2010) attributed the origins of dolomite and ankerite to hydrothermal fluids. Moreover, a biogenic origin of Mg-bearing minerals in the lake was also proposed (Nyirő-Kósa et al., 2018). Degradation of algae in a reducing environment would have released Mg^{2+} and Ca^{2+} that can be then incorporated into the Mg-bearing minerals (Desborough, 1978). In this case, the source of Fe^{2+} for siderite likely derived from the illitization of smectite and lithoclasts. Hence, in this study, the possible sources for Mg-bearing and Mg, Fe-bearing minerals include: i) algae in the lake and ii) hydrothermal fluids (Yuan et al., 2019; Zhang et al., 2020). Dolomite was likely precipitated below the sulphur reduction zone (Coleman, 1985). The fining upwards beds indicate that this facies was possibly deposited from density flows or turbidity currents. The calcareous shale has the highest content of calcite cements and less pores. Moreover, this facies was locally developed and interbedded with siliceous shales in the studied well (Fig. 13(c)).

Lenticular fabric is common in carbonate, clay and silt-bearing shale. The origin of this fabric is interpreted as water-rich shale intraclasts transported into the bed, representing the transport of muds by currents (Schieber et al., 2010; Davies et al., 2012; Newport et al., 2018). The fabric is elongated and aligned to the bedding with distinct boundaries. Parallel laminations suggest periods of hemipelagic deposition (Fig. 13(c)). The deposition of organic-rich carbonate, clay and silt-bearing shale may be in the tails of turbidity flows (Kneller and McCaffrey, 2003). Compared to

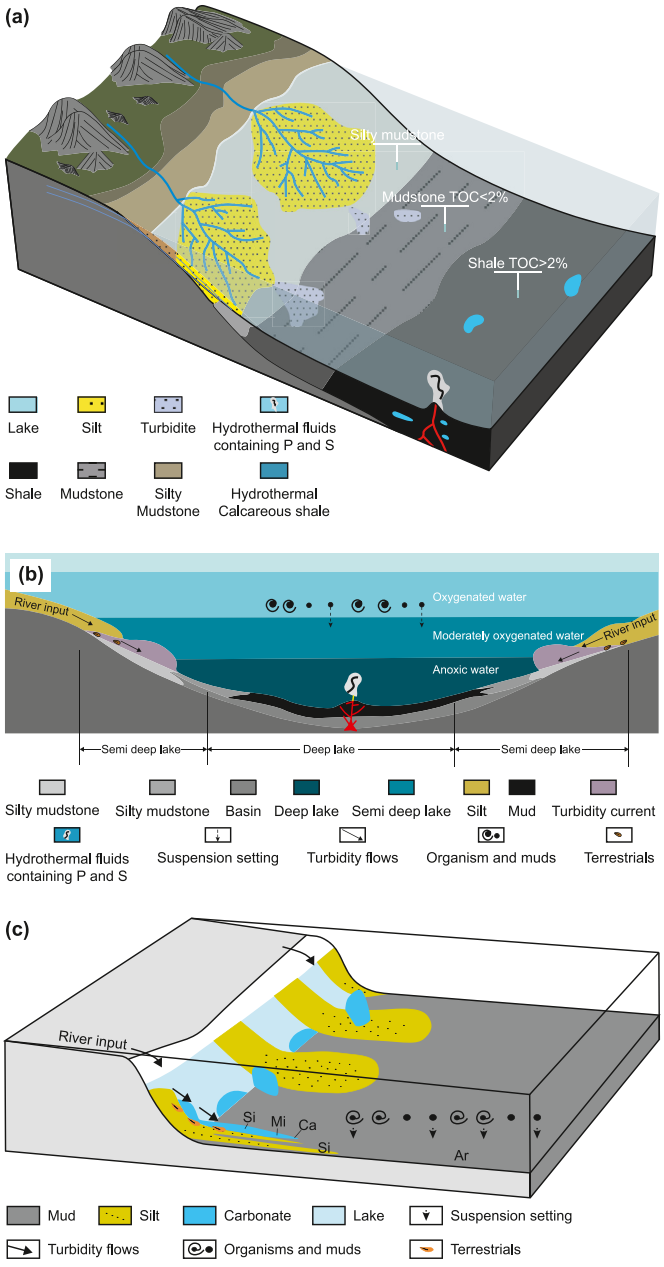

Fig. 13. A 3D and 2D schematic summary of the depositional environment of lacustrine shale from the Yanchang Formation. **(a)** 3D schematic figure showing the input sources of lacustrine shales. Silt grains were transported by river into the lake, forming silty mudstone, mudstone and shales. **(b)** Three layers of lake water including oxygenated water, moderately oxygenated water and anoxic water were formed from the top to the bottom owing to the varied river input, corresponding to shallow, semi-deep and deep lake environment respectively. **(c)** The sketch of depositional environment of lacustrine shale from the Yanchang Formation. Ca: calcareous shale; Mi: mixed shale, that is carbonate, clay and silt-bearing shale; Si: siliceous shale; Ar: argillaceous shale. Siliceous shale was likely deposited due to low density flows (turbidity). Calcareous shales were possibly formed owing the mixture of the deep hydrothermal water, which brought large amounts of calcium and magnesium ions, and lake water. Argillaceous shale was mainly deposited from suspension in a deep lake environment, however, some silt grains and carbonates can be input by debris flows and density flows. Carbonate, clay and silt-bearing shale was deposited due to the density flows and can be found near the base. The possible depositional areas of different shale types are marked.

siliceous shale, carbonate, clay and silt-bearing shale contains more organic pores within organic matter and intra- and inter-mineral pores around and within mixed layer clay minerals and silicates. Intra- organic pores and inter-minerals pores are two main types of pores for gas and oil migration, they are likely connected to provide pathways for fluid and gas transport. Moreover, in this shale type, Facies 1 (argillaceous siliceous shale) has the highest TOC content. High TOC contents suggest high productivity in the basin during these times. The value of V/(V + Ni) in the studied shale samples are over 0.6, suggesting that these shales were deposited in an anoxic bottom sediments (Hatch and Leventhal, 1992; Rimmer, 2004) (Fig. 13(b)). Previous studies have reported that the flux of P diffusing from sediments elevated at the anoxic bottom water conditions, which resulted in the increase in productivity during that period (Peng et al., 2021; Yuan et al., 2021). Volcanic and hydrothermal activities that occurred during the deposition of lacustrine shale in the Yanchang Formation also provided the nutrient for the bioproductivity (Zhang et al., 2017) (Fig. 13(b)). The long-term anoxic reducing conditions at the bottom of the lake basin allowed the preservation of algal organic matter. Hence, this facies is a potential source rock for shale oil.

5.2. Paragenetic sequence

There are many diagenetic minerals in the studied samples. However, the main diagenetic processes in each shale facies are different (Fig. 14). Argillaceous shale is characterised by the abundant of clay minerals such as kaolinite, illite and illite/smectite mixed layer clay minerals. Quartz content is less than other shale types. Hence, the main diagenetic process in this shale type is dominated by the formation of kaolinite and the transformation between clay minerals. The illitization of kaolinite was observed in the studied samples, and hence kaolinite was formed before clay minerals transformation as shown in Fig. 14. Physical compaction has a strongly negative impact on the primary porosity of shales. Based on a mathematical model, the porosity of shale has been shown to abruptly decreases from over 60% to 20% during early diagenetic physical compaction (Lee et al., 2020). The presence of deformation structures around detrital grains and organic matter indicate that the compaction after the deposition (Fig. 7). Fig. 14 shows the decrease in porosity after the deposition. The formation of kaolinite can decrease the shale porosity and permeability (Mondol, 2009). Illitization of smectite commonly occurs at the late burial stage in shale (Hower et al., 1976; Bjorkum and Gjelsvik, 1988; Boles and Franks, 1979; Froelich et al., 1979; Bjørlykke and Aagaard, 1992; Peltonen et al., 2009). Pores in this facies type mainly preserved between clay minerals and muscovite planes. Hence, the transformation of clay mineral has slightly effect on porosity after deep burial stage.

In siliceous shales, calcite cements were precipitated around quartz grains (Fig. 8(e) and (f)), which caused the decrease in shale porosity. Dolomite and ankerite were formed in the matrix and within muscovite planes after the precipitation of calcite (SEM images in Fig. 3). The main diagenetic process in this shale type is the pressure-dissolution of quartz and formation of quartz overgrowth (Fig. 10(a) and (d)). Based on the measured Tmax data, the average converted vitrinite reflectance of the studied sample is 0.82%. This indicates that the organic matter is oil-mature and the studied samples are in the deep burial diagenetic stage. The release of organic-acid fluids generated during the maturation of organic matter contributes to the dissolution of quartz and feldspar (Baruch et al., 2015). The secondary pores were likely produced after the release of organic acid during this diagenetic stage. Illitization of smectite provides a possible source for quartz overgrowth (Bjorkum and Gjelsvik, 1988; Peltonen et al., 2009; Thyberg et al., 2010; Dowey and Taylor, 2017; Peng et al., 2020). Hence, the illitization of smectite occurred before the precipitation of quartz overgrowth. Quartz overgrowth around detrital grains reduces the shale porosity.

In calcareous shales, diagenetic processes are dominated by the formation of carbonates including calcite, dolomite, ankerite and siderite. Their cementation can reduce shale porosity. The volume of mesopores is higher than that of macropores. The pores were mainly caused by the dissolution of carbonate cements.

In carbonate, clay and silt-bearing shales, the dissolution of K-feldspar was found in this shale facies. The precipitation of authigenic feldspar in the dissolved area was observed (Fig. 14), indicating that the dissolution of K-feldspar occurred before the transformation of clay minerals. The illitization of kaolinite can be found in Fig. 11(a). The presence of dissolved K-feldspar provides a possible source for illitization of kaolinite at a temperature range from 70 to 130 °C (Bjorkum and Gjelsvik, 1988; Burley and Macquaker, 1992). The increase of clay contents (e.g., kaolinite and illite) can also reduce the porosity of shales.

5.3. Prediction of 'sweet-spots'

High organic matter input and good preservation conditions are important for the development of good shale oil reservoirs. Organic matter is well preserved in argillaceous, siliceous shales and some carbonate, clay and silt-bearing shales, owing to their interpreted anoxic environment of deposition. The Vr_{eq} converted from the T_{max} data shows that argillaceous, siliceous and calcareous shale has reached the oil window and in the peak oil section (0.8–1). Some of carbonate, clay and silt-bearing shale samples are in the peak oil section as well, while some of them are in the immature and early oil window. Based on the TOC, Vr_{eq} and depositional environment, Facies 1 (argillaceous siliceous shale) in carbonate, clay and silt-bearing shale type is interpreted as a good source rock for shale oil in this system. Organic pores and some intra-mineral pores in carbonate, clay and silt-bearing indicates the migration of organic acid from this shale facies of shale. Hence, carbonate, clay and silt-bearing shale provides a possible pathway for shale oil migration and also likely serves as a source rock for shale oil. Siliceous shale with inter-mineral pores likely acts as reservoirs for shale oil. Argillaceous shale contains much more clay minerals than other shale types. Such a high percentage of clay minerals can reduce the porosity and permeability of shale, and therefore argillaceous shale is also a prospective internal seal for shale oil. Therefore, the interbedded layers of Ar (the argillaceous shale) and Mi (mixed shale-carbonate, clay and silt-bearing shale) are considered as the best shale oil target horizons.

6. Conclusion

(1) Based on microfacies and compositional analysis, the oil-bearing shale within the Chang 7 Member of the Yanchang Formation in the Ordos Basin is divided into argillaceous shale; siliceous shale; calcareous shale; and carbonate-, clay- and silt-bearing shale. These microfacies were the product of varying depositional processes, productivity and water column conditions.

(2) Diagenetic minerals across all samples include pyrite, calcite, dolomite, ankerite, siderite, quartz, kaolinite, illite and illite/smectite mixed-layers. In many samples cementation by carbonate and quartz can be extensive, but also common is the dissolution of calcite and quartz, replacement of feldspar by kaolinite, as well as the transformation of smectite to illite. The transformation from smectite to illite provided a possible source for the formation of diagenetic quartz. The

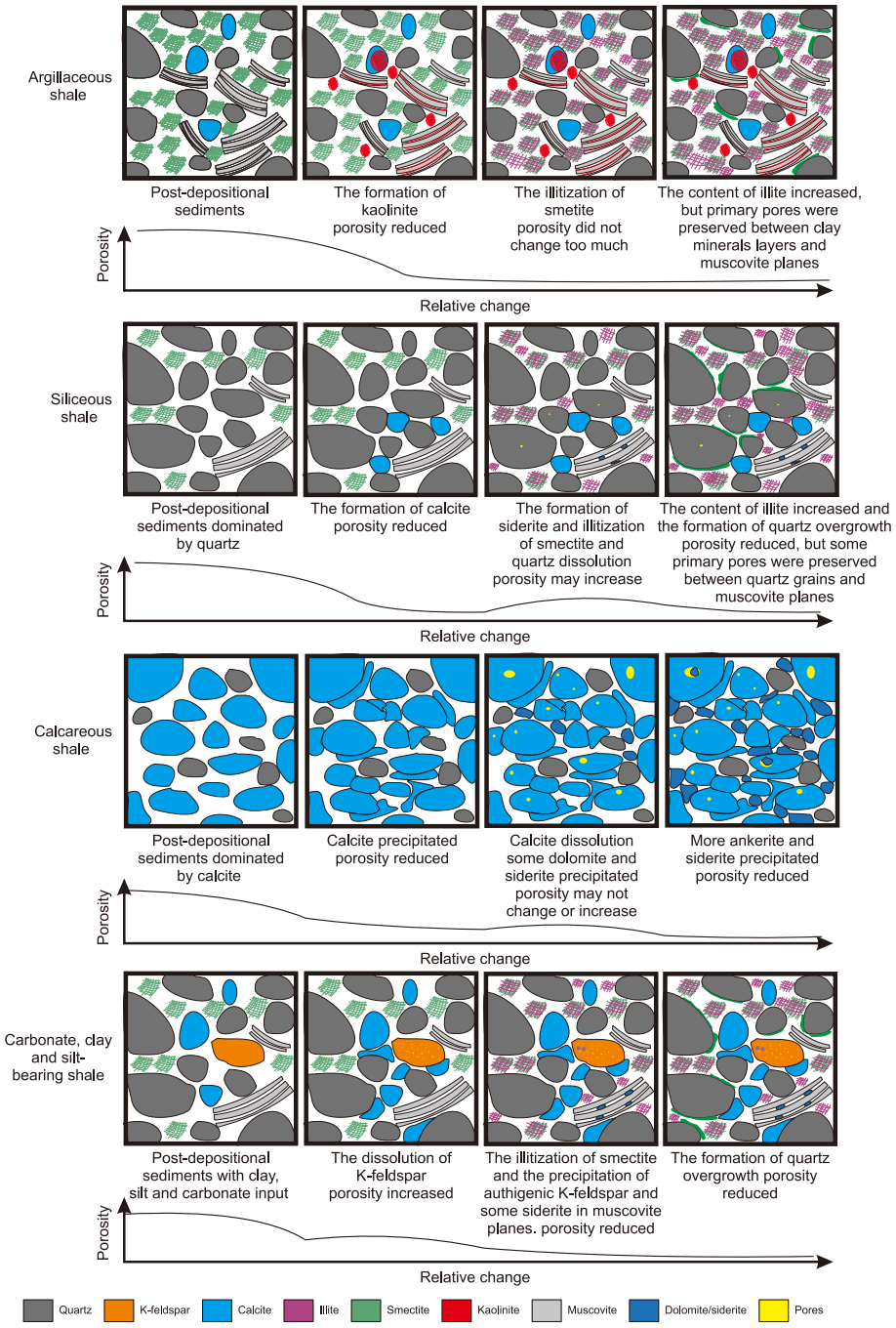

Fig. 14. Schematic illustrations of main diagenetic processes in the four shale types with the relative porosity changes.

formation of non-ferroan and ferroan dolomite is likely related to lake-water chemistry and/or the presence of hydrothermal fluids.

(3) In carbonate-, clay- and silt-bearing shale type, the subfacies named argillaceous siliceous shale is likely to have generated most hydrocarbon. Argillaceous shale type has greater clay mineral contents and lower volumes of mesopores than the siliceous and calcareous shales, and therefore argillaceous shale is predicted to have lower permeability and likely to act as an effective internal seal to oil. Siliceous shale has the highest pore volume and many inter-mineral pores, which can be considered as the potential reservoir for shale oil.

CRediT authorship contribution statement

Bin Bai: Conceptualization, Methodology, Investigation, Data curation, Writing – original draft. **Jing-Yue Hao:** Methodology, Investigation, Data curation, Writing – original draft. **Ling Fu:** Investigation, Data curation. **Yu-Xi Liu:** Investigation, Data curation. **Jian-Peng Wang:** Conceptualization, Methodology, Investigation, Data curation, Writing – review & editing. **Lan Wang:** Investigation, Data curation. **Kevin G. Taylor:** Methodology, Investigation, Writing – review & editing. **Lin Ma:** Conceptualization, Methodology, Investigation, Writing – review & editing.

Declaration of competing interest

The authors declare the following financial interests/personal relationships which may be considered as potential competing interests: Bin Bai reports financial support was provided by National Natural Science Foundation of China, Department of Chemical Sciences, Division of Environmental Chemistry. Bin Bai reports financial support was provided by National Science and technology major project. Bin Bai reports financial support was provided by science and technology research project of PetroChina Company Limited. Jing-Yue Hao reports financial support was provided by China Scholarship Council. Jian-Peng Wang reports financial support was provided by International Postdoctoral Exchange Fellowship Program. Lin Ma reports financial support was provided by Natural Environment Research Council.

Acknowledgement

This study was founded by National Natural Science Foundation of China (grant Nos.: 42072186 and 42090025), National Science and Technology Major Project, China (grant No.: 2016ZX05046-001) and Science and Technology Research Project of PetroChina Company Limited, China (grant No.: 2021DJ1806). Jing-Yue Hao wishes to acknowledge the fund support from China Scholarship Council (No. 201806440002). Jian-Peng Wang would like to acknowledge the International Postdoctoral Exchange Fellowship Program, China (Talent-Introduction Program, No. 270152) and Lin Ma wishes to acknowledge the fund support from Natural Environment Research Council, United Kingdom (NE/R013527/1).

References

Bai, Y., Ma, Y.H., 2020. Geology of the Chang 7 member oil shale of the Yanchang Formation of the Ordos Basin in central north China. Petrol. Geosci. 26, 355–371. https://doi.org/10.1144/petgeo2018-091.

Baruch, E.T., Kennedy, M.J., Löhr, S.C., Dewhurst, D.N., 2015. Feldspar dissolution-enhanced porosity in paleoproterozoic shale reservoir facies from the Barney Creek formation (McArthur basin, Australia). AAPG (Am. Assoc. Pet. Geol.) Bull. 99, 1745–1770. https://doi.org/10.1306/04061514181.

Bjorkum, P.A., Gjelsvik, N., 1988. An isochemical model for formation of authigenic kaolinite, K-feldspar and illite in sediments. J. Sediment. Res. 58, 506–511. https://doi.org/10.1306/212F8DD2-2B24-11D7-8648000102C1865D.

Bjørlykke, K., Aagaard, P., 1992. Clay Minerals in North Sea Sandstones. https://doi.org/10.2110/pec.92.47.0065.

Boles, J.R., Franks, S.G., 1979. Clay diagenesis in Wilcox sandstones of Southwest Texas; implications of smectite diagenesis on sandstone cementation. J. Sediment. Res. 49, 55–70.

Burley, S.D., Macquaker, J.H., 1992. Authigenic Clays Diagenetic Sequences and Conceptual Diagenetic Models in Contrasting Basin-Margin and Basin-Center North Sea Jurassic Sandstones and Mudstones. SEPM Special Publication No 47, 81–110. https://doi.org/10.2110/pec.92.47.0081.

Chen, L., Jiang, Z.X., Liu, Q.X., Jiang, S., Liu, K.Y., Tan, J.Q., Gao, F.L., 2019. Mechanism of shale gas occurrence: insights from comparative study on pore structures of marine and lacustrine shales. Mar. Petrol. Geol. 104, 200–216. https://doi.org/10.1016/j.marpetgeo.2019.03.027.

Chen, S.B., Han, Y.F., Fu, C.Q., Zhu, Y.M., Zuo, Z.X., 2016. Micro and nano-size pores of clay minerals in shale reservoirs: implication for the accumulation of shale gas. Sediment. Geol. 342, 180–190. https://doi.org/10.1016/j.sedgeo.2016.06.022.

Coleman, M., 1985. Geochemistry of diagenetic non-silicate minerals: kinetic considerations. Phil. Trans. Roy. Soc. Lond. Math. Phys. Sci. 315, 39–56. https://doi.org/10.1098/rsta.1985.0028.

Davies, S., Leng, M., Macquaker, J., Hawkins, K., 2012. Sedimentary process control on carbon isotope composition of sedimentary organic matter in an ancient shallow-water shelf succession. G-cubed 13. https://doi.org/10.1029/2012GC004218.

Desborough, G.A., 1978. A biogenic-chemical stratified lake model for the origin of oil shale of the Green River Formation: an alternative to the playa-lake model. Geol. Soc. Am. Bull. 89, 961–971. https://doi.org/10.1130/0016-7606(1978)89<961:ABSLMF>2.0.CO;2.

Dowey, P.J., Taylor, K.G., 2017. Extensive authigenic quartz overgrowths in the gas-bearing Haynesville-Bossier Shale, USA. Sediment. Geol. 356, 15–25. https://doi.org/10.1016/j.sedgeo.2017.05.001.

Duan, Y., Wang, C.Y., Zheng, C.Y., Wu, B.X., Zheng, G.D., 2008. Geochemical study of crude oils from the Xifeng oilfield of the Ordos Basin, China. J. Asian Earth Sci. 31, 341–356. https://doi.org/10.1016/j.jseaes.2007.05.003.

Duan, Y., Yuan, Y.D., Qian, R.R., 2013. Migration features of crude oil in fluvial deposits of Maling oilfield in Ordos Basin, China. Org. Geochem. 58, 78–85. https://doi.org/10.1016/j.orggeochem.2013.02.011.

Franks, S.G., Zwingmann, H., 2010. Origin and timing of late diagenetic illite in the Permian–Carboniferous Unayzah sandstone reservoirs of Saudi Arabia. AAPG Bull. 94, 1133–1159. https://doi.org/10.1306/04211009142.

Froelich, P.N., Klinkhammer, G., Bender, M.L., Luedtke, N., Heath, G.R., Cullen, D., Dauphin, P., Hammond, D., Hartman, B., Maynard, V., 1979. Early oxidation of organic matter in pelagic sediments of the eastern equatorial Atlantic: suboxic diagenesis. Geochem. Cosmochim. Acta 43, 1075–1090. https://doi.org/10.1016/0016-7037(79)90095-4.

Gamero-Diaz, H., Miller, C., Lewis, R., 2012. sCore: a classification scheme for organic mudstones based on bulk mineralogy. Search and Discovery article, 40951.

Gingras, M.K., Pemberton, S.G., Smith, M., 2015. Bioturbation: reworking sediments for better or worse. Oilfield Rev. 26, 46–58.

Guo, Q.L., Yao, Y., Hou, L.H., Tang, S.H., Pan, S.Q., Yang, F., 2022. Oil migration, retention, and differential accumulation in “sandwiched” lacustrine shale oil systems from the Chang 7 member of the Upper Triassic Yanchang Formation, Ordos Basin, China. Int. J. Coal Geol. 261, 104077. https://doi.org/10.1016/j.coal.2022.104077.

Hao, J., Ma, L., Hollis, C., Fauchille, A.-L., Taylor, K.G., 2023. Spatial distribution of mineral development in Carboniferous Bowland Shale, UK at 3D micro-to nano-scales. Int. J. Coal Geol. 104236.

Hao, J., Taylor, K.G., Hollis, C., 2021. Mineral diagenesis and inferred fluids in basinal mudstones: The Carboniferous Morridge Formation, Widmerpool Gulf, UK. Marine and Petrol. Geol. 134, 105373.

Hatch, J., Leventhal, J., 1992. Relationship between inferred redox potential of the depositional environment and geochemistry of the upper Pennsylvanian (missourian) Stark shale member of the dennis limestone, Wabaunsee county, Kansas, USA. Chem. Geol. 99, 65–82. https://doi.org/10.1016/0009-2541(92)90031-Y.

He, C., Ji, L.M., Su, A., Wu, Y.D., Zhang, M.Z., Zhou, S.X., Li, J., Hao, L.W., Ma, Y., 2019. Source-rock evaluation and depositional environment of black shales in the Triassic Yanchang Formation, southern Ordos Basin, north-central China. J. Petrol. Sci. Eng. 173, 899–911. https://doi.org/10.1016/j.petrol.2018.10.089.

Hower, J., Eslinger, E.V., Hower, M.E., Perry, E.A., 1976. Mechanism of burial metamorphism of argillaceous sediment: 1. Mineralogical and chemical evidence. Geol. Soc. Am. Bull. 87, 725–737. https://doi.org/10.1130/0016-7606(1976)87<725:MOBMOA>2.0.CO;2.

Hu, S.Y., Zhao, W.Z., Hou, L.H., Yang, Z., Zhu, R.K., Wu, S.T., Bai, B., Jin, X., 2020. Development potential and technical strategy of continental shale oil in China. Petrol. Explor. Dev. 47, 877–887. https://doi.org/10.1016/S1876-3804(20)60103-3.

Hua, Y., Liang, X., Xiaobing, N., Shengbin, F., Yuan, Y., 2017. Geological conditions for continental tight oil formation and the main controlling factors for the enrichment: A case of Chang 7 Member, Triassic Yanchang Formation, Ordos Basin, NW China. Petrol. Explor. Dev. 44, 11–19.

Jarvie, D., Claxton, B., Henk, F., Breyer, J., 2001. Oil and Shale Gas fromBarnett Shale, Ft. Worth Basin, Texas. AAPG Annual Meeting Program. https://doi.org/10.1306/8626E28D-173B-11D7-8645000102C1865D.

Jarvie, D.M., 2012. Shale Resource Systems for Oil and Gas: Part 2—Shale-Oil Resource Systems. https://doi.org/10.1306/13321447M973489.

Ji, L.M., Yan, K., Meng, F.W., Zhao, M., 2010. The oleaginous Botryococcus from the Triassic Yanchang Formation in Ordos Basin, northwestern China: morphology and its paleoenvironmental significance. J. Asian Earth Sci. 38, 175–185. https://doi.org/10.1016/j.jseaes.2009.12.010.

Johnson, E.A., Liu, S., Zhang, Y., 1989. Depositional environments and tectonic controls on the coal-bearing lower to Middle Jurassic Yan'an formation, southern Ordos Basin, China. Geology 17, 1123–1126. https://doi.org/10.1130/0091-7613(1989)017<1123:DEATCO>2.3.CO;2.

Kneller, B.C., McCaffrey, W.D., 2003. The interpretation of vertical sequences in turbidite beds: the influence of longitudinal flow structure. J. Sediment. Res. 73, 706–713. https://doi.org/10.1306/031103730706.

Könitzer, S.F., Davies, S.J., Stephenson, M.H., Leng, M.J., 2014. Depositional controls on mudstone lithofacies in a basinal setting: implications for the delivery of sedimentary organic matter. J. Sediment. Res. 84, 198–214. https://doi.org/10.2110/jsr.2014.18.

Lazar, O.R., Bohacs, K.M., Schieber, J., Macquaker, J.H., Demko, T.M., 2015. Mudstone Primer: Lithofacies Variations, Diagnostic Criteria, and Sedimentologic-Stratigraphic Implications at Lamina to Bedset Scales. SEPM (Society for Sedimentary Geology. https://doi.org/10.2110/SEPMCSP.12.

Lee, E.Y., Novotny, J., Wagreich, M., 2020. Compaction trend estimation and applications to sedimentary basin reconstruction (BasinVis 2.0). Appl. Comput. Geosci. 5, 100015. https://doi.org/10.1016/j.acags.2019.100015.

Liang, C., Cao, Y.C., Liu, K.Y., Jiang, Z.X., Wu, J., Hao, F., 2018. Diagenetic variation at the lamina scale in lacustrine organic-rich shales: implications for hydrocarbon migration and accumulation. Geochem. Cosmochim. Acta 229, 112–128. https://doi.org/10.1016/j.gca.2018.03.017.

Lin, C.M., Wang, B.J., Zhang, X., Zhang, N., Jiang, K.X., Huang, S.Y., Cai, M.J., 2019. Geological characteristics and paleoenvironmental significance of the paleogene lacustrine dolomite in the Beitang Sag, Bohai Bay basin. Geol. J. China Univ. 25, 377. https://doi.org/10.16108/j.issn1006-7493.2019010.

Liu, B., Teng, J., Li, C., Li, B.Q., Bie, S.Z., Wang, Y.L., 2022a. The control of shale composition on the pore structure characteristics of lacustrine shales: a case

study of the Chang 7 member of the Triassic Yanchang Formation, Ordos Basin, north China. Energies 15, 8353. https://doi.org/10.3390/en15228353.
Liu, B., Wang, Y., Tian, S.S., Guo, Y.L., Wang, L., Yasin, Q., Yang, J.G., 2022b. Impact of thermal maturity on the diagenesis and porosity of lacustrine oil-prone shales: insights from natural shale samples with thermal maturation in the oil generation window. Int. J. Coal Geol. 261, 104079. https://doi.org/10.1016/j.coal.2022.104079.
Liu, H.M., Zhang, S., Song, G.Q., Wang, X.J., Teng, J.B., Wang, M., Bao, Y.S., Yao, S.P., Wang, W.Q., Zhang, S.P., Hu, Q.H., Fang, Z.W., 2019. Effect of shale diagenesis on pores and storage capacity in the Paleogene Shahejie formation, Dongying depression, Bohai Bay basin, east China. Mar. Petrol. Geol. 103, 738–752. https://doi.org/10.1016/j.marpetgeo.2019.01.002.
Ma, L., Dowey, P.J., Rutter, E., Taylor, K.G., Lee, P.D., 2019. A novel upscaling procedure for characterising heterogeneous shale porosity from nanometer-to millimetre-scale in 3D. Energy 181, 1285–1297.
Ma, L., Slater, T., Dowey, P.J., Yue, S., Rutter, E.H., Taylor, K.G., Lee, P.D., 2018. Hierarchical integration of porosity in shales. Sci. Rep. 8, 1–14.
Ma, L., Taylor, K.G., Dowey, P.J., Courtois, L., Gholinia, A., Lee, P.D., 2017. Multi-scale 3D characterisation of porosity and organic matter in shales with variable TOC content and thermal maturity: examples from the Lublin and Baltic Basins, Poland and Lithuania. Int. J. Coal Geol. 180, 100–112.
Ma, L., Taylor, K.G., Lee, P.D., Dobson, K.J., Dowey, P.J., Courtois, L., 2016. Novel 3D centimetre-to nano-scale quantification of an organic-rich mudstone: The Carboniferous Bowland Shale, Northern England. Marine and Petrol. Geol. 72, 193–205.
Maugeri, L., 2013. The Shale Oil Boom: a US Phenomenon. Harvard Kennedy School, Belfer Center for Science and International Affairs.
Milliken, K.L., Esch, W.L., Reed, R.M., Zhang, T., 2012. Grain assemblages and strong diagenetic overprinting in siliceous mudrocks, Barnett shale (Mississippian), Fort Worth basin, Texas. AAPG Bull. 96, 1553–1578. https://doi.org/10.1306/12011111129.
Mondol, N.H., 2009. Porosity and permeability development in mechanically compacted silt-kaolinite mixtures. SEG Technical Program Expanded Abstracts 2009. Society of Exploration Geophysicists, pp. 2139–2143. https://doi.org/10.1190/1.3255280.
Mondol, N.H., Bjørlykke, K., Jahren, J., Høeg, K., 2007. Experimental mechanical compaction of clay mineral aggregates—changes in physical properties of mudstones during burial. Mar. Petrol. Geol. 24, 289–311. https://doi.org/10.1016/j.marpetgeo.2007.03.006.
Newport, S.M., Jerrett, R.M., Taylor, K.G., Hough, E., Worden, R.H., 2018. Sedimentology and microfacies of a mud-rich slope succession: in the Carboniferous Bowland basin, NW England (UK). J. Geol. Soc. 175, 247–262. https://doi.org/10.1144/jgs2017-036.
Nyirő-Kósa, I., Rostási, Á., Bereczk-Tompa, É., Cora, I., Koblar, M., Kovács, A., Pósfai, M., 2018. Nucleation and growth of Mg-bearing calcite in a shallow, calcareous lake. Earth Planet Sci. Lett. 496, 20–28. https://doi.org/10.1016/j.epsl.2018.05.029.
Peltonen, C., Marcussen, Ø., Bjørlykke, K., Jahren, J., 2009. Clay mineral diagenesis and quartz cementation in mudstones: the effects of smectite to illite reaction on rock properties. Mar. Petrol. Geol. 26, 887–898. https://doi.org/10.1016/j.marpetgeo.2008.01.021.
Peng, J.W., 2021. Sedimentology of the Upper Pennsylvanian organic-rich Cline Shale, Midland Basin: from gravity flows to pelagic suspension fallout. Sedimentology 68, 805–833. https://doi.org/10.1111/sed.12811.
Peng, J.W., Fu, Q.L., Larson, T.E., Janson, X., 2021. Trace-elemental and petrographic constraints on the severity of hydrographic restriction in the silled Midland Basin during the late Paleozoic ice age. GSA Bull. 133, 57–73. https://doi.org/10.1130/B35336.1.
Peng, J.W., Hu, Z.Q., Feng, D.J., Wang, Q.R., 2022. Sedimentology and sequence stratigraphy of lacustrine deep-water fine-grained sedimentary rocks: the lower Jurassic Dongyuemiao Formation in the Sichuan basin, Western China. Mar. Petrol. Geol. 146, 105933. https://doi.org/10.1016/j.marpetgeo.2022.105933.
Peng, J.W., Hu, Z.Q., Feng, D.J., Wang, Q.R., 2023. Variations of organic matter content and type within the sequence stratigraphic framework of the lacustrine deep-water Dongyuemiao formation, Sichuan Basin, Western China. Mar. Petrol. Geol., 106104 https://doi.org/10.1016/j.marpetgeo.2023.106104.
Peng, J.W., Milliken, K.L., Fu, Q.L., 2020. Quartz types in the Upper Pennsylvanian organic-rich Cline Shale (Wolfcamp D), Midland Basin, Texas: implications for silica diagenesis, porosity evolution and rock mechanical properties. Sedimentology 67, 2040–2064. https://doi.org/10.1111/sed.12694.
Qiu, X.W., Liu, C.Y., Mao, G.Z., Deng, Y., Wang, F.F., Wang, J.Q., 2014. Late Triassic tuff intervals in the Ordos Basin, Central China: their depositional, petrographic, geochemical characteristics and regional implications. J. Asian Earth Sci. 80, 148–160. https://doi.org/10.1016/j.jseaes.2013.11.004.
Rimmer, S.M., 2004. Geochemical paleoredox indicators in Devonian–Mississippian black shales, central Appalachian Basin (USA). Chem. Geol. 206, 373–391. https://doi.org/10.1016/j.chemgeo.2003.12.029.
Ross, D.J., Bustin, R.M., 2009. The importance of shale composition and pore structure upon gas storage potential of shale gas reservoirs. Mar. Petrol. Geol. 26, 916–927. https://doi.org/10.1016/j.marpetgeo.2008.06.004.
Schieber, J., Southard, J.B., Schimmelmann, A., 2010. Lenticular shale fabrics resulting from intermittent erosion of water-rich muds—interpreting the rock record in the light of recent flume experiments. J. Sediment. Res. 80, 119–128. https://doi.org/10.2110/jsr.2010.005.
Schwartz, B., Huffman, K., Thornton, D., Elsworth, D., 2019. The effects of mineral distribution, pore geometry, and pore density on permeability evolution in gas shales. Fuel 257, 116005. https://doi.org/10.1016/j.fuel.2019.116005.
Teng, J., Deng, H.C., Liu, B., Chen, W.L., Fu, M.Y., Xia, Y., Yu, H.Z., 2021. Insights of the pore system of lacustrine shales from immature to late mature with the aid of petrology, mineralogy and porosimetry: a case study of the Triassic Yanchang Formation of the Ordos Basin, North China. J. Petrol. Sci. Eng. 196, 107631. https://doi.org/10.1016/j.petrol.2020.107631.
Thyberg, B., Jahren, J., Winje, T., Bjørlykke, K., Faleide, J.I., Marcussen, Ø., 2010. Quartz cementation in Late Cretaceous mudstones, northern North Sea: changes in rock properties due to dissolution of smectite and precipitation of micro-quartz crystals. Mar. Petrol. Geol. 27, 1752–1764. https://doi.org/10.1016/j.marpetgeo.2009.07.005.
Wang, K., Chandler, M., Wang, J., Dowey, P., Storm, M., Taylor, K.G., Lee, P., Ma, L., 2021a. Time-lapse nanometre-scale 3D synchrotron imaging and image-based modelling of the response of shales to heating. Int. J. Coal. Geol. 103816.
Wang, E.Z., Feng, Y., Guo, T.L., Li, M.W., 2022. Oil content and resource quality evaluation methods for lacustrine shale: a review and a novel three-dimensional quality evaluation model. Earth Sci. Rev., 104134 https://doi.org/10.1016/j.earscirev.2022.104134.
Wang, M., Guo, Z.Q., Jiao, C.X., Lu, S.F., Li, J.B., Xue, H.T., Li, J.J., Li, J.Q., Chen, G.H., 2019. Exploration progress and geochemical features of lacustrine shale oils in China. J. Petrol. Sci. Eng. 178, 975–986. https://doi.org/10.1016/j.petrol.2019.04.029.
Wang, K., Taylor, K.G., Ma, L., 2021b. Advancing the application of atomic force microscopy (AFM) to the characterization and quantification of geological material properties. Int. J. Coal. Geol. 247, 103852.
Wei, W., Algeo, T.J., 2020. Elemental proxies for paleosalinity analysis of ancient shales and mudrocks. Geochem. Cosmochim. Acta 287, 341–366. https://doi.org/10.1016/j.gca.2019.06.034.
Xu, Q.L., Zhao, X.Z., Pu, X.G., Han, W.Z., Shi, Z.N., Tian, J.Q., Zhang, B.J., Xin, B.X., Guo, P.F., 2021. Characteristics and control mechanism of lacustrine shale oil reservoir in the member 2 of Kongdian Formation in Cangdong Sag, Bohai Bay basin, China. Front. Earth Sci. 1144. https://doi.org/10.3389/feart.2021.783042.
Yang, H., Niu, X.B., Xu, L.M., et al., 2016. Exploration potential of shale oil in Chang7 member, upper Triassic Yanchang formation, Ordos Basin, NW China. Petrol. Explor. Dev. 43, 560–569.
Yang, Y.T., Li, W., Ma, L., 2005. Tectonic and stratigraphic controls of hydrocarbon systems in the Ordos basin: a multicycle cratonic basin in central China. AAPG Bull. 89, 255–269. https://doi.org/10.1306/10070404027.
Yang, Y.Y., Liu, Y.Q., Šegvić, B., Zhou, D.W., You, J.Y., Jiao, X., Meng, Z.Y., Zhao, M.R., 2023. Origin, transport, and diagenesis of tuffs in organic-rich lacustrine mudstone: an example from the lower part of the Middle–Late Triassic Chang7 Member, Ordos Basin (NW China). Appl. Clay Sci. 232, 106790. https://doi.org/10.1016/j.clay.2022.106790.
Yang, Z., Zou, C.N., Wu, S.T., Lin, S.H., Pan, S.Q., Niu, X.B., Men, G.T., Tang, Z.X., Li, G.H., Zhao, J.H., Jia, X.Y., 2019. Formation, distribution and resource potential of the “sweet areas (sections)” of continental shale oil in China. Mar. Petrol. Geol. 102, 48–60. https://doi.org/10.1016/j.marpetgeo.2018.11.049.
Yuan, W., Liu, G.D., Bulseco, A., Zhou, X.X., 2021. Iron speciation in organic-rich shales from the upper Triassic Yanchang Formation, Ordos Basin, northern China: implications for depositional environment. J. Asian Earth Sci. 220, 104917. https://doi.org/10.1016/j.jseaes.2021.104917.
Yuan, W., Liu, G.D., Xu, L.M., Niu, X.B., Li, C.Z., 2019. Petrographic and geochemical characteristics of organic-rich shale and tuff of the Upper Triassic Yanchang Formation, Ordos Basin, China: implications for lacustrine fertilization by volcanic ash. Can. J. Earth Sci. 56, 47–59. https://doi.org/10.1139/cjes-2018-0123.
Zhang, K., Liu, R., Liu, Z.J., Li, B.L., Han, J.B., Zhao, K.G., 2020. Influence of volcanic and hydrothermal activity on organic matter enrichment in the Upper Triassic Yanchang Formation, southern Ordos Basin, Central China. Mar. Petrol. Geol. 112, 104059. https://doi.org/10.1016/j.marpetgeo.2019.104059.
Zhang, L.F., Sun, M., Wang, S.G., Yu, X.Y., 1998. The composition of shales from the Ordos basin, China: effects of source weathering and diagenesis. Sediment. Geol. 116, 129–141. https://doi.org/10.1016/S0037-0738(97)00074-2.
Zhang, W.Z., Yang, H., Xie, L.Q., Yang, Y.H., 2010. Lake-bottom hydrothermal activities and their influence on high-quality source rock development: a case from Chang 7 source rocks in Ordos Basin. Petrol. Explor. Dev. 37, 424–429. https://doi.org/10.1016/S1876-3804(10)60043-2.
Zhang, W.Z., Yang, W.W., Xie, L.Q., 2017. Controls on organic matter accumulation in the Triassic Chang 7 lacustrine shale of the Ordos Basin, central China. Int. J. Coal Geol. 183, 38–51. https://doi.org/10.1016/j.coal.2017.09.015.
Zhang, Z.L., Sun, K.Q., Yin, J.R., 1997. Sedimentology and sequence stratigraphy of the Shanxi Formation (Lower Permian) in the northwestern Ordos Basin, China: an alternative sequence model for fluvial strata. Sediment. Geol. 112, 123–136. https://doi.org/10.1016/S0037-0738(97)00029-8.
Zhao, W.Z., Hu, S.Y., Hou, L.H., Yang, T., Li, X., Guo, B.C., Yang, Z., 2020. Types and resource potential of continental shale oil in China and its boundary with tight oil. Petrol. Explor. Dev. 47, 1–11. https://doi.org/10.1016/S1876-3804(20)60001-5.
Zou, C.N., Yang, Z., Cui, J.W., Zhu, R.K., Hou, L.H., Tao, S.Z., Yuan, X.J., Wu, S.T., Lin, S.H., Wang, L., Bai, B., Yao, J.L., 2013. Formation mechanism, geological characteristics and development strategy of nonmarine shale oil in China. Petrol. Explor. Dev. 40, 15–27. https://doi.org/10.1016/S1876-3804(13)60002-6.